Supplement of Atmos. Chem. Phys., 25, 16679–16695, 2025 https://doi.org/10.5194/acp-25-16679-2025-supplement © Author(s) 2025. CC BY 4.0 License.





Supplement of

Measurement report: Anthropogenic activities reduction suppresses HONO formation: direct evidence for secondary pollution control

Mingzhu Zhai et al.

Correspondence to: Shengrui Tong (tongsr@iccas.ac.cn) and Maofa Ge (gemaofa@iccas.ac.cn)

The copyright of individual parts of the supplement might differ from the article licence.

Text S1 NO₂ correction

As the most important precursor of HONO, accurate measurement of NO₂ was crucial for analyzing HONO formation. A commercial Thermo Scientific analyzer (42i) used in this study could specifically detect NO. The measurement of NO₂ was achieved by converting NO₂ to NO through a molybdenum converter. However, the chemiluminescence (CL) technique could overestimate NO₂ concentrations because of the interference of NOy. These interferences included HONO, HNO₃, HNO₄, N₂O₅, NO₃, peroxyacetyl nitrate (PANs, RC(O)OONO₂), organic nitrates (RONO₂), and peroxynitrates (ROONO₂) (Villena et al., 2012; Wu et al., 2022). Therefore, the NO₂ measured by the CL-NOx analyzer represented the sum of real NO₂ and these interfering species. In contrast, the commercial Teledyne API-N500 NOx analyzer was based on cavity attenuated phase shift (CAPS) technique. It could provide direct absorption measurement of NO₂ at 450 nm in the blue region of the electromagnetic spectrum, allowed fast and accurate detection of NO₂ without interference from water vapor. The only known potential interferences in the typical ambient environment were dicarbonyl compounds such as glyoxal and methylglyoxal, whose concentrations were usually much lower than NO₂ mixing ratios (Kebabian et al., 2008). Therefore, NO₂ measured by the CAPS-NOx analyzer (CAPS-NO₂) could be used to correct the NO₂ measured by the CL-NOx analyzer (CL_NO₂).

We conducted a NO_2 field campaign at the ICCAS site from September 19 to October 11, 2023, to compare the performance of the CL-NOx and CAPS-NOx analyzers. The sampling inlets of both instruments were placed at the same location, with identical sampling tube lengths, and the analyzers were housed in the same indoor environment to minimize external interference. The results showed that $CAPS_NO_2$ and CL_NO_2 exhibited similar temporal variations (Figure S1(a) and S1(b)). Notably, CL_NO_2 was consistently higher than $CAPS_NO_2$, with a more pronounced difference during the daytime. This discrepancy was mainly attributed to elevated NOy concentrations caused by enhanced photochemical reactions. Consequently, the fraction of $CAPS_NO_2$ in CL_NO_2 displayed a distinct diurnal pattern, being higher at night and lower during the day (Figure S1(c)), which was consistent with previous findings (Xue et al., 2022; Zhang et al., 2022c). Based on this result, we applied separate calibrations for daytime (07:00-18:00 LT) and nighttime (19:00-next 06:00 LT) data. The results indicated strong linear correlations between $CAPS_NO_2$ and CL_NO_2 during both periods ($R^2 = 0.96$ for daytime and $R^2 = 0.95$ for nighttime). The regression equations were "y = 0.98x - 2.27" for daytime and

"y = 0.99x - 2.29" for nighttime, where y represented CAPS_NO₂ and x represented CL_NO₂ (Figure S1(d) and S1(e)). Using these relationships to correct the NO₂ data obtained in this study provided a more reasonable estimation of true NO₂ concentrations and offered a reliable basis for further analysis.

Text S2 Special event on December 12 from 5:00-23:00 LT

During the observation period, a special event was noted from 5:00–23:00 LT on December 12, during which particulate matter concentrations exhibited abnormally high values, with PM_{2.5} and PM₁₀ concentrations reaching 318 μg m⁻³ and 1410 μg m⁻³, respectively. Concurrently, the WS and RH remained within normal ranges, consistent with other time periods. The concentrations of additional pollutants (O₃, CO, and SO₂) obtained at the Wanliu monitoring station of the Beijing Environmental Monitoring Station did not exhibit similar elevations. This pattern suggested that the abrupt increase in PM_{2.5} and PM₁₀ concentrations may have been attributable to local emission sources. After excluding this specific event, the data was further analyzed.

Text S3 General analysis of related air pollutants and meteorological parameters

Throughout the entire observation period, there was a significant temperature (Temp) variation due to span across two seasons, ranging from -9.44 °C to 30.92 °C, with an average of 10.62 ± 8.68 °C. Similarly, the relative humidity (RH) also exhibited a wide range of variation, and was noticeably higher at nighttime than at daytime, ranging from 6.89 % to 83.86 %, with an average of 34.03 ± 17.61 %. The photolysis frequency of HONO (j_{HONO}) gradually decreased from the beginning to the end of the observation, indicating that solar radiation diminished from autumn to winter, which was also illustrated by the photolysis frequencies of NO_2 (j_{NO2}) and O_3 (j_{O1D}) (Figure S2). The average concentrations of $PM_{2.5}$ and PM_{10} in this observation were 38.25 ± 39.49 μg m⁻³ and 72.48 ± 56.98 μg m⁻³, respectively. The hourly concentration of NO and NO_2 ranged from below the detection limit to maximum values of 97.53 ppb and 84.60 ppb, with average values of 8.60 ± 13.44 ppb and 19.64 ± 17.63 ppb, respectively. NH_3 and CO exhibited similar trends during the observation period, suggesting a common source for them in urban areas, predominantly attributed to vehicle emissions and haze pollution (Xu et al., 2023; Sun et al., 2017; Meng et al., 2011). The hourly concentrations of NH_3 ranged from 4.18 to 75.63 ppb, with an average of 17.25 ± 9.90 ppb. And the hourly concentrations of CO ranged from 0.08 to 1.51 ppm,

with an average of 0.44 ± 0.28 ppm. The concentration of SO_2 remained at a low level in this measurement, with hourly concentrations consistently below 4 ppb and an average of 0.90 ± 0.47 ppb. Since SO_2 served as a tracer for coal combustion (Zhang et al., 2022b), the low levels of SO_2 in this study indicated that the impact of coal combustion could be negligible in urban area of Beijing. The hourly concentrations of O_3 had a range of 0.46–126.19 ppb, with an average of 16.78 ± 18.78 ppb, which was significantly lower than O_3 concentrations in Beijing during the summer (Li et al., 2021; Xue et al., 2021). This was attributed to the reduced light intensity and diminished photochemical formation of O_3 in autumn and winter.

The diurnal variations of chemical species (HONO, NO, NO₂, NH₃, CO, O₃, PM_{2.5}) and meteorological parameters (Temp, RH) during DHP, PEP and CLP were illustrated in Figure 2. The concentration comparison of the main species during three periods was shown in Table S1 in the Supporting Information. Since the observation period spanned both autumn and winter, the mean Temp during the three periods gradually decreased (22.87 \pm 4.12 °C in DHP, 13.07 \pm 4.28 °C in PEP, and 0.02 \pm 4.45 °C in CLP), which was also reflected in the gradual decrease of the solar radiation intensity, join (Figure S4). The diurnal variation of Temp remained consistent across three periods, with Temp gradually increasing after sunrise, peaking in the afternoon (14:00-15:00 LT), then decreasing to reach the minimum values around sunrise. However, due to seasonal differences, the time of the lowest temperature (i.e., sunrise time) varied among the three periods, being around 6:30 LT in DHP, around 7:00 LT in PEP, and around 8:00 LT in CLP. The delay in sunrise time across the three periods was also observed in the diurnal variations of joid and RH. The diurnal variations in RH were consistent across all three periods, displaying a pattern inverse to that of Temp, with higher RH at night and lower during the day. Notably, the average RH was similar during DHP ($40.71 \pm 18.45\%$) and PEP ($39.60 \pm 17.23\%$), whereas it decreased by 50 % in CLP (19.94 \pm 6.40 %). The average WS during the three periods was similar, maintaining at a low level (< 0.7 m s⁻¹), and showing consistent diurnal variation, with higher during the day and lower at night. The characteristics of low WS and high RH enhanced atmospheric stability and reduced air mixing, which may lead to the accumulation of pollutants near the ground, making them difficult to disperse (Wang et al., 2017b; Xu et al., 2019).

Text S4 Calculation of direct HONO emission factor

It is commonly accepted that the $\Delta HONO/\Delta NOx$ ratio in freshly released air masses can represent the direct emission factor of HONO (EF_{emis}) (Zhang et al., 2020; Meng et al., 2020). Previous studies have obtained a wide range of EF_{emis} (0.1–2.1 %) (Yang et al., 2014; Liu et al., 2017; Kurtenbach et al., 2001; Rappengluck et al., 2013), influenced by many factors such as vehicle types, fuel composition, and engine types. Therefore, to assess the impact of vehicle emissions in this observation, the local emission factor EF_{emis} (= $\Delta HONO/\Delta NOx$) was derived based on ambient measurements. Considering the possibility of secondary HONO formation from aging air masses during the transport process, six criteria were used to ensure that the selected air masses were as fresh as possible:

- 1) Only nighttime data (from 19:00 LT to next 06:00 LT), to avoid photochemical reactions of HONO (Li et al., 2012; Meng et al., 2020).
- 2) NO > 20 ppb, to ensure the existence of obvious vehicle emissions (Su et al., 2008b).
- 3) Sharp NOx peaks with $\Delta NO/\Delta NOx > 0.9$, along with strong positive-relationships between NO and NOx (correlation coefficient, $R^2 > 0.9$), to convince that the air mass was almost fresh (Liu et al., 2019; Xu et al., 2015).
- 4) Strong positive-relationships between HONO and NOx ($R^2 > 0.8$) to ensure HONO was closely related to vehicle emissions (Xu et al., 2015).
- 5) The duration of the air mass was less than 1 hour, minimizing the impact of HONO secondary production (Meng et al., 2020).
- 6) The WS was less than 2 m s⁻¹, and there was no precipitation, in order to mitigate the influence of transport processes and wet deposition (Yun et al., 2017).

Figure S6 displayed three fresh plumes observed on 1 to 2 November 2022 based on the preceding selection criteria. In these cases, high $\Delta NO/\Delta NOx$ ratios (1.19, 1.08, and 1.01) and good correlations between HONO and NOx (R²=0.97, 0.85, and 0.94) were observed. The slopes of the linear regression between HONO and NOx were considered the emission factor EF_{emis} (Rappengluck et al., 2013), with the emission factor EF_{emis} of 0.0164, 0.0143, and 0.0206 for the two cases. According to these criteria, a total of 21 fresh air masses were identified during the observation period and summarized in Table S2. The ΔHONO/ΔNOx ratios in these selected air masses ranged from 0.0051 to 0.0210.

Text S5 Calculation of NO₂ uptake coefficient on the surfaces

In previous studies, the uptake coefficient of NO₂ (γ) on the ground and aerosol surfaces varied widely under different laboratory conditions, ranging from 10⁻⁸ to 10⁻³ (George et al., 2005; Kleffmann et al., 1998; Wong et al., 2011; Colussi et al., 2013). It was challenging to determine which γ was more representative in the real atmospheric conditions. Therefore, it was necessary to obtain an appropriate γ to adapt to the surrounding environment being analyzed. Based on the current observations, we planned to choose ideal air masses where heterogeneous reactions of NO₂ only occur at the ground surface to quantify the γ at the ground surface. The data involved in the calculation process needed to meet the following criteria:

- 1) Only nighttime data (from 19:00 LT to next 06:00 LT) was considered to avoid complex photochemical reactions and ensure a stable boundary layer height.
- 2) Wind speeds were kept below 2 m s⁻¹ to ensure stable conditions with minimal horizontal and vertical transport.
- 3) The concentration of NO was maintained below 10 ppb to mitigate the impact of homogeneous reactions between NO and OH.
- 4) The concentration of $PM_{2.5}$ was kept below 20 μg m⁻³ to minimize the influence of heterogeneous reactions of NO_2 on aerosol surfaces.
- 5) Continuously increasing HONO, with a positive correlation between HONO and NO₂, where the correlation coefficient (R²) was greater than 0.6, ensuring that HONO originated from the heterogeneous conversion of NO₂.

Based on the criteria above, to further understand the heterogeneous conversion of NO_2 to HONO at night and to correct for the influences of other sources and diffusion processes, the conversion frequency of NO_2 to HONO (k_{het}) was calculated using the following formula. It was assumed that all measured HONO originated from the heterogeneous conversion of NO_2 (Wang et al., 2017a; Su et al., 2008a; Xuan et al., 2023).

$$\begin{split} k_{HONO}^{X} = & \frac{2\left(\frac{[HONO_{corr}]_{t2}}{[X]_{t2}} \times [\overline{X}] - \frac{[HONO_{corr}]_{t1}}{[X]_{t1}} \times [\overline{X}]\right)}{(t_2 - t_1)\left(\frac{[NO_2]_{t2}}{[X]_{t2}} \times [\overline{X}] + \frac{[NO_2]_{t1}}{[X]_{t1}} \times [\overline{X}]\right)} = \frac{2\left(\frac{[HONO_{corr}]_{t2}}{[X]_{t2}} - \frac{[HONO_{corr}]_{t1}}{[X]_{t1}}\right)}{(t_2 - t_1)\left(\frac{[NO_2]_{t2}}{[X]_{t2}} + \frac{[NO_2]_{t1}}{[X]_{t1}}\right)} \\ k_{het} = & \frac{1}{3}(k_{HONO}^0 + k_{HONO}^{COO} + k_{HONO}^{NO2}) \end{split}$$

where, $[HONO_{corr}]_t$, $[NO_2]_t$, and $[X]_t$ respectively represented the concentrations of $HONO_{corr}$, NO_2 and the reference gases (CO and NO_2) at time t. $[\overline{X}]$ was the average concentration of the reference gases during the time intervals t_1 and t_2 . k_{HONO}^X was the conversion frequency scaled with the reference gases. k_{HONO} was calculated by combining k_{HONO}^0 (not scaled k_{HONO}), k_{HONO}^{CO} (CO scaled k_{HONO}) and $k_{HONO}^{NO_2}$ (NO₂ scaled k_{HONO}), reducing the impact of uncertainties from emissions and diffusion processes on the conversion frequency.

A total of 12 cases of the heterogeneous processes on the ground surfaces had been selected. The average value of $k_{\text{het-g}}$ was 0.0101 $h^{\text{-1}}$.

k_{het-g} at the ground surface could also be expressed by the following formula.

$$k_{het-g} = \frac{1}{8} \times \sqrt{\frac{8RT}{\pi M}} \times \frac{1}{MLH} \times \gamma_g$$

where, R was the ideal gas constant (J mol⁻¹ K⁻¹), T was the temperature in Kelvin (K), M was the molecular mass of NO₂ (kg mol⁻¹), and MLH was the mixed layer height of HONO (m). γ_g represented the uptake coefficient of NO₂ at the ground surfaces. The average value of obtained γ_g was 2.94×10⁻⁶, which was comparable to previous studies (Alicke, 2002; Yu et al., 2022b).

The conversion frequency (k_{het-a}) and uptake coefficient of NO_2 (γ_a) on aerosol surfaces were calculated using the same method. Based on the following criteria, only ideal air masses featuring heterogeneous reactions of NO_2 on aerosol surfaces were included in the analysis.

- 1) Only nighttime data (from 19:00 LT to next 06:00 LT) was considered to avoid complex photochemical reactions and ensure a stable boundary layer height.
- 2) Wind speeds were kept below 2 m s⁻¹ to ensure stable conditions with minimal horizontal and vertical transport.
- 3) The concentration of NO was maintained below 10 ppb to mitigate the impact of homogeneous reactions between NO and OH.
- 4) The concentration of $PM_{2.5}$ was kept above 20 μg m⁻³ to make sure that the heterogeneous reactions of NO_2 happened on aerosol surfaces.
- 5) Continuously increasing HONO, with a positive correlation between HONO and NO₂, where the correlation coefficient (R²) was greater than 0.6, ensuring that HONO originated from the heterogeneous conversion of NO₂.

Based on the above criteria, a total of 13 ideal cases of heterogeneous conversion occurring on aerosol surfaces were selected. The average value of k_{het-a} was $0.006 \, h^{-1}$.

 $k_{\text{het-a}}$ at the aerosol surfaces could also be expressed by the following formula.

$$k_{\text{het-a}} = \frac{1}{8} \times \sqrt{\frac{8RT}{\pi M}} \times SA \times \gamma_a$$

$$SA=60.03 \times PM_{2.5}^{0.62}$$

where, SA represented the surface area of aerosols (m² m⁻³). Since SA was not measured in this observation, it was calculated by using empirical formula (Zhang et al., 2022c; Cai et al., 2017). After subtracting the impact of NO_2 heterogeneous reactions at the ground surface, the average of γ_a was 3.12×10^{-5} . This was comparable to γ_a obtained by Zhang et al. during haze periods in Beijing (Zhang et al., 2023).

For the photo-enhanced NO₂ uptake coefficient on ground surfaces ($\gamma_{g,hv}$) took the same value as γ_g , and for the aerosol surface uptake coefficient ($\gamma_{a,hv}$) also took the same value as γ_a . Laboratory studies had shown that solar irradiance could enhance the heterogeneous conversion of NO₂ to HONO on various surfaces (Yu et al., 2022a; George et al., 2005). Therefore, the photo-enhanced reaction during the daytime was scaled using the photo-enhanced factor $\frac{j_{NO2}}{0.005\,\text{s}^{-1}}$. The frequency of conversion of NO₂ on a wide range of surfaces (k_{het}) results from the combination of the MLH, NO₂ uptake coefficients, and the HONO yield. Although there is currently some uncertainty in obtaining appropriate NO₂ uptake coefficients for real atmospheres, k_{het} values derived from our observations are relatively reliable and are a useful method for obtaining appropriate NO₂ conversion frequencies during in situ observations.

Text S6 The specific parameter values for the production and removal pathways of HONO

According to previous research, the average dry deposition velocity of HONO (v_{HONO}) was taken as 2 cm s⁻¹ (Harrison et al., 1996). The BLH was obtained from the ECMWF website (https://www.ecmwf.int/), as illustrated in Figure S8 in the Supplementary Information. According to Text S5, the values of γ_g and $\gamma_{g,hv}$ were set to 2.94×10^{-6} , while the values of γ_a and $\gamma_{a,hv}$ were set to 3.12×10^{-5} . The average molecular speed of NO_2 (v_{NO2}) was calculated using the formula $v_{NO2} = \sqrt{\frac{8RT}{\pi M}}$. MLH denoted the mixing layer height of HONO, typically ranging from 25 to 100 m (Xue et al., 2022; Zhang et al., 2022c). MLH was considered significantly lower than BLH because HONO was formed

from the local and ground-level sources and had a short lifetime, which could be confirmed through gradient measurements (Meng et al., 2020; He et al., 2023; Ryan et al., 2018; Zhu et al., 2011). A HONO gradient study in Leshan, Sichuan Province, indicated that HONO was mainly localized, with concentrations rapidly decreasing from 4.8 ppb at ground level to below 0.2 ppb at 300 m (Xing et al., 2021). Based on previous studies (Lee et al., 2016; Xue et al., 2020; Xue et al., 2022), MLH was taken as 50 m in this observation to assess the ground-level sources of HONO.

EF represented the enhancement factor of the photolysis rate of pNO₃ relative to that of HNO₃. Laboratory studies reported EF values between 1 and 700 for aerosols (Romer et al., 2018; Ye et al., 2016; Ye et al., 2017), and experimental values up to 1700 for urban grime (Baergen and Donaldson, 2013). However, EF is widely considered to carry substantial uncertainty, which can translate into uncertainty in HONO concentrations. In this study, we adopted a moderate EF (=30) commonly used for autumn in Beijing (Zhang et al., 2022a; Xuan et al., 2024). In addition, to comprehensively evaluate the potential impact of EF uncertainty on the results, a sensitivity analysis was conducted by decreasing and increasing the EF by one order of magnitude (i.e., EF=3 and EF=300). The corresponding changes in HONO concentrations during the three periods were summarized in Table S3. When EF=3, the changes were approximately 3.2 %, 3.4 %, and 2.1 % during DHP, PEP, and CLP, respectively, indicating that the variation in the contribution of pNO₃ photolysis to HONO formation was negligible compared with that under EF = 30. In contrast, when EF=300, the changes were 31.5 %, 34.1 %, and 20.5 %, respectively, suggesting that the contribution of pNO₃ photolysis to HONO formation increased slightly relative to the EF=30. These results demonstrated that the EF value could influence the contribution of pNO₃ photolysis to HONO formation, highlighting the importance of EF in quantitatively constraining the HONO budget. The reliability of model simulation results was typically evaluated using the Index of Agreement (IOA), and its calculation formula was as follows (Liu et al., 2022; Hu et al., 2023):

$$IOA=1-\frac{\sum_{i=1}^{n}(S_{i}-O_{i})^{2}}{\sum_{i=1}^{n}\left(|S_{i}-\overline{O}|+|O_{i}-\overline{O}|\right)^{2}}$$

where, S_i represented the simulated values, O_i was the observed values, \overline{O} was the average of the observed values, and n was the number of samples. The IOA ranged from 0–1, with higher values indicating better consistency between the simulated and observed values. In this study, the IOA for HONO simulation was 0.92, which was within the range of previous studies (Wang et al., 2018;

Ghahremanloo et al., 2021). Thus, the simulation results of HONO using this Box model were deemed acceptable.

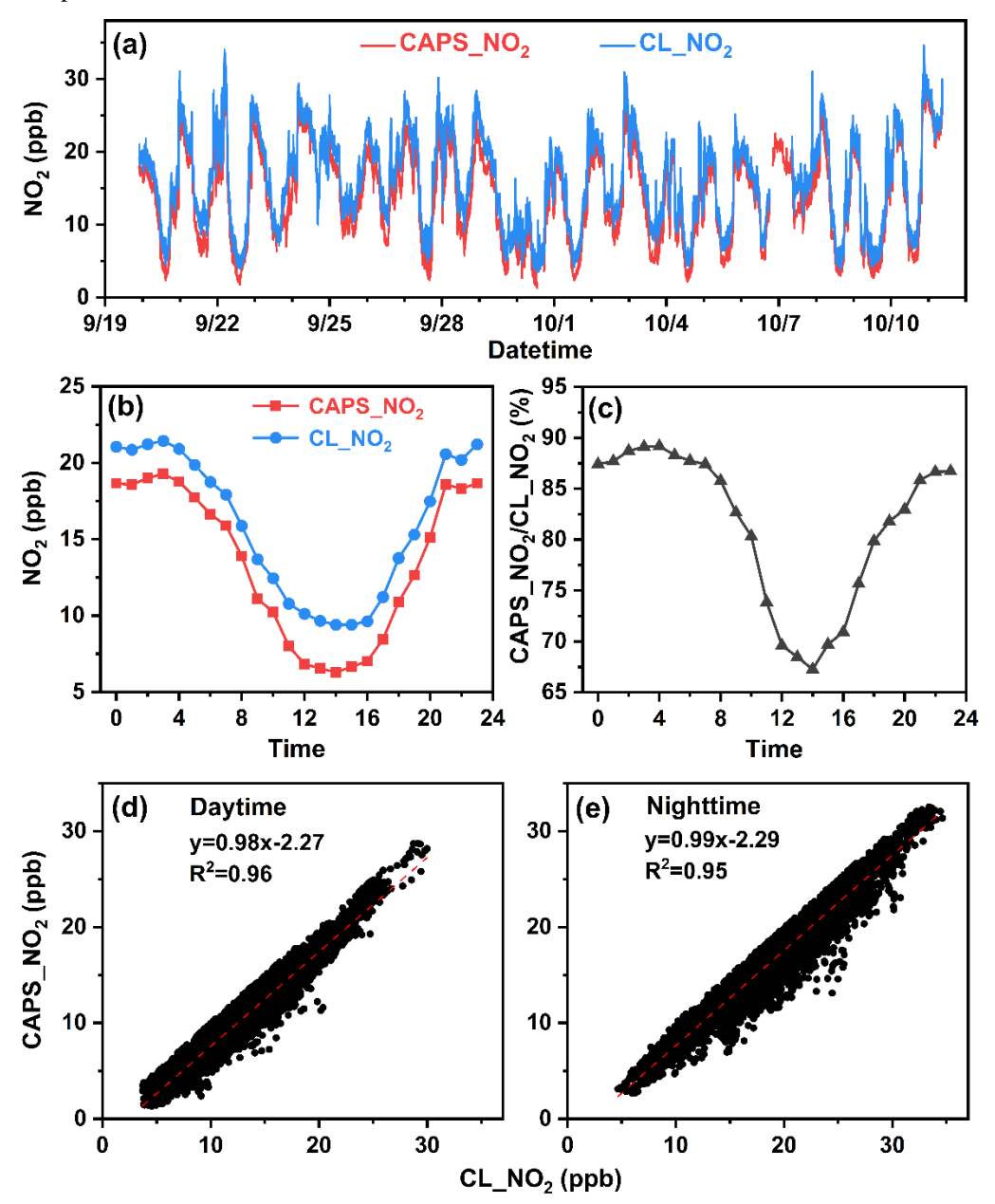


Figure S1 Time series (a) and diurnal variations (b) of CAPS_NO₂ and CL_NO₂, the diurnal variations of the fraction of CAPS_NO₂ in CL_NO₂ (c), and scatter plots with linear fits of CAPS_NO₂ versus CL_NO₂ during daytime (d) and nighttime (e).

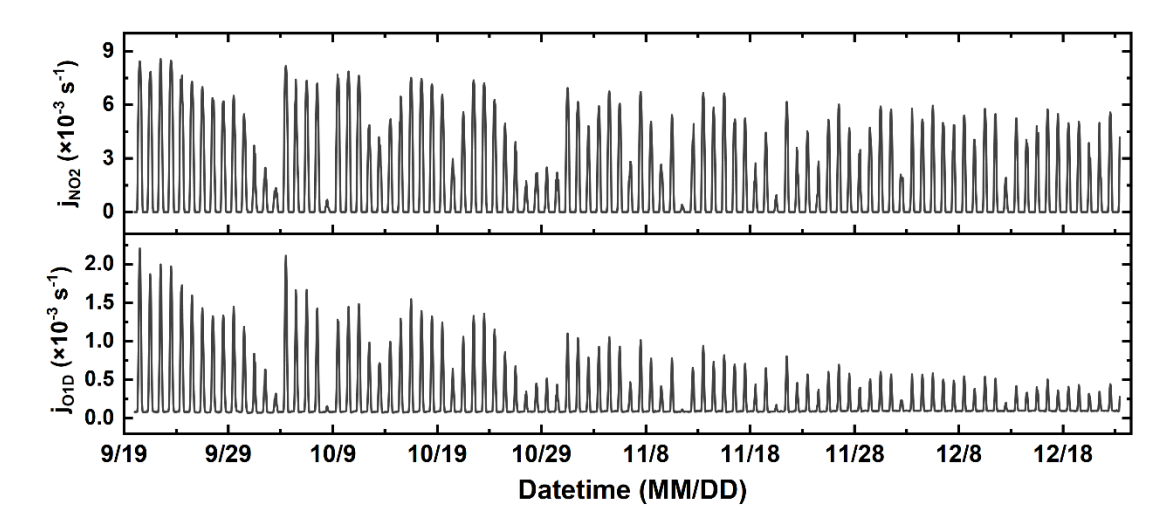


Figure S2 Hourly time series of the photolysis frequencies of NO_2 (j_{NO2}) and O_3 (j_{O1D}) from 20 September to 23 December 2022. The j_{NO2} and j_{O1D} decreased gradually from the beginning to the end of the observation, indicating a gradual weakening of solar radiation from autumn to winter.

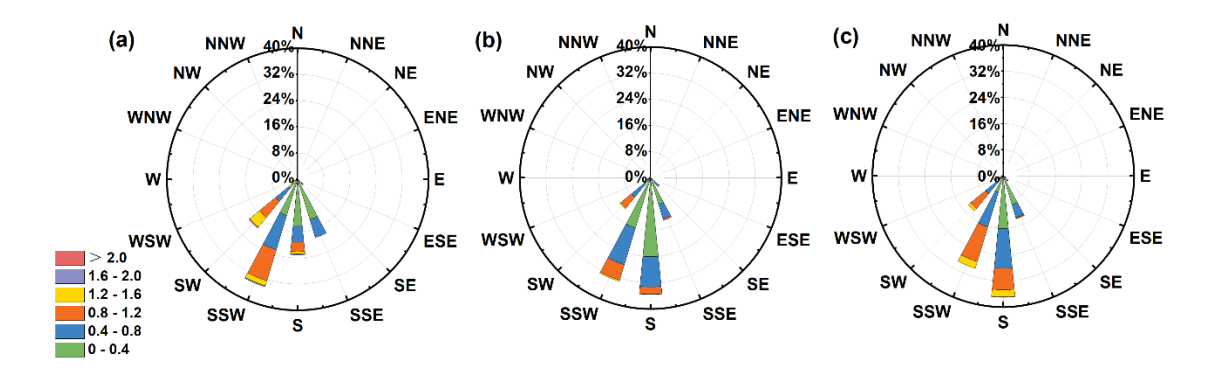


Figure S3 The wind rose diagrams for the (a) DHP, (b) PEP, and (c) CLP. The wind speed was represented by color shading. The south wind was the dominant wind direction during all three periods, with wind speeds consistently below 2 m s⁻¹. These conditions were typical of the stagnant meteorological conditions in Beijing.

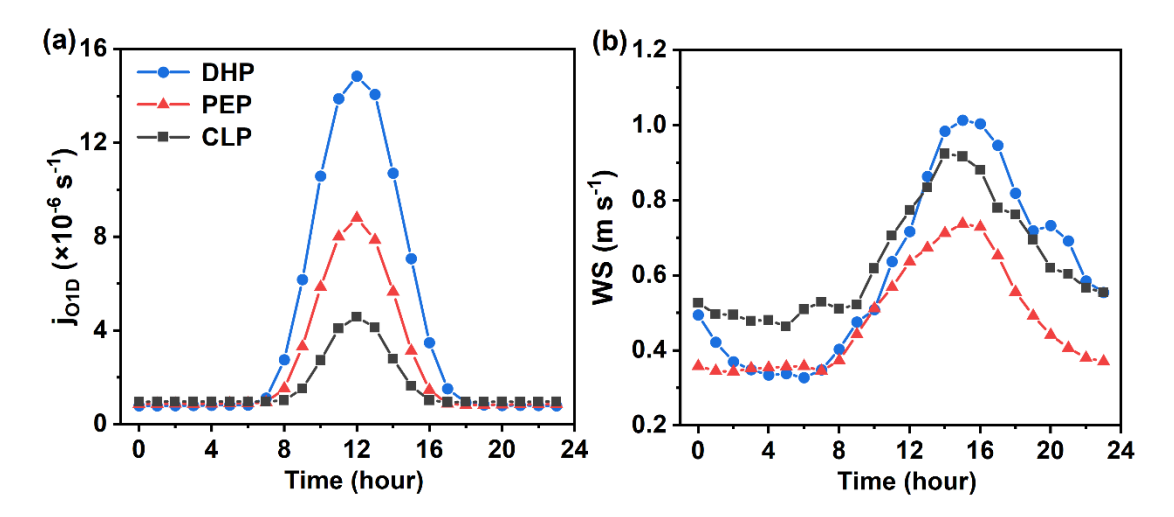


Figure S4 The diurnal variations of j_{O1D} and WS during three periods. The blue, red, and black dotted line graphs represent DHP, PEP and CLP, respectively.

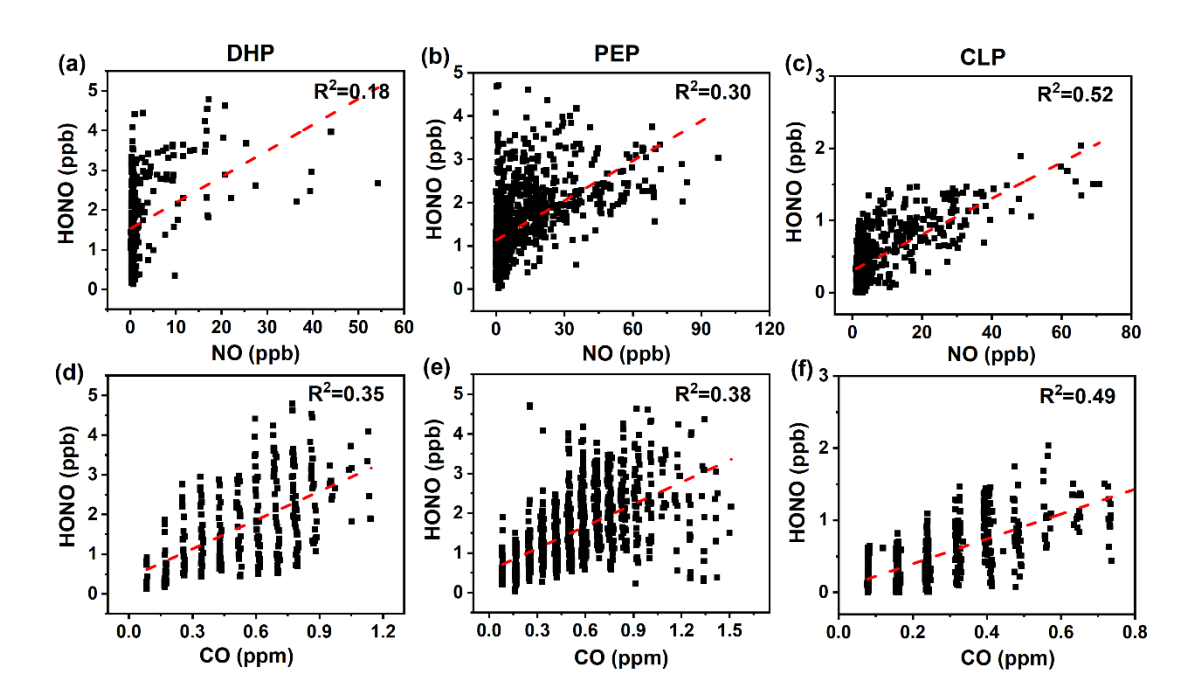


Figure S5 Correlations of HONO with NO and CO during the DHP (a, d), PEP (b, e) and CLP (c, f). The red dashed lines were obtained by the linear fits from the scatters data. The data had a temporal resolution of 1 hour.

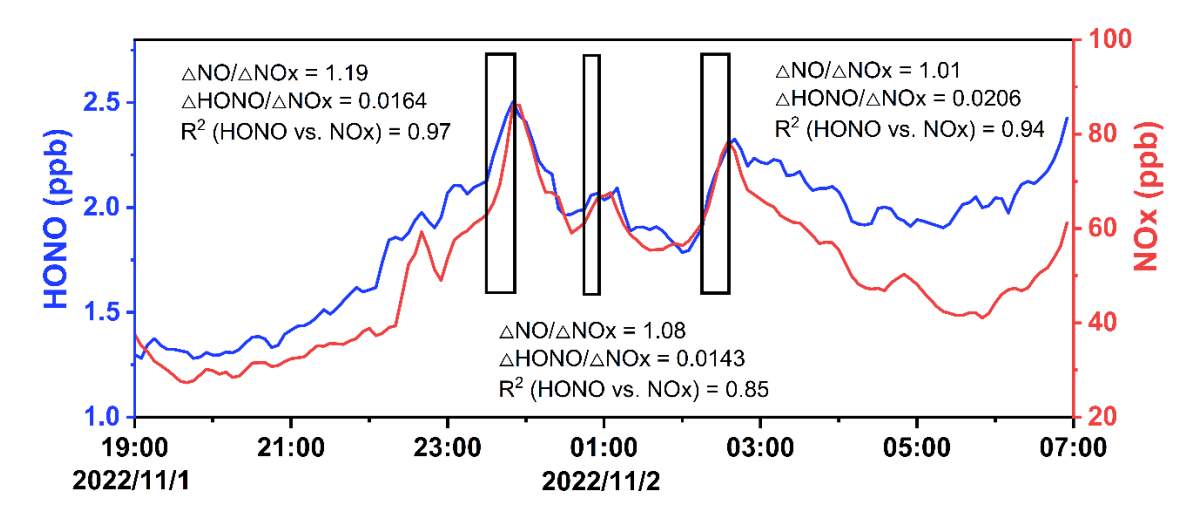


Figure S6 Hourly time series of the concentration of HONO and NOx on 1 to 2 November 2022. The region marked by the black frames indicated three fresh plumes. The HONO emission ratios were estimated using the data collected in the black frames.

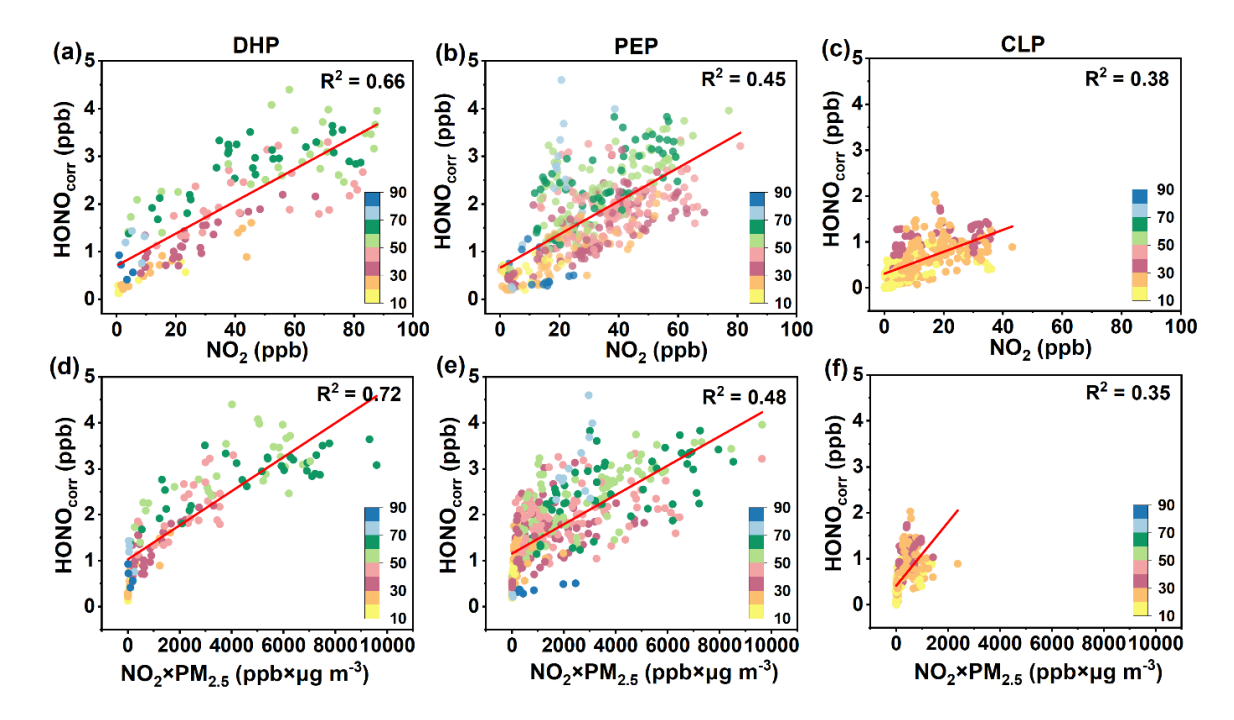


Figure S7 The correlations between $HONO_{corr}$ and NO_2 (a–c), $HONO_{corr}$ and $NO_2 \times PM_{2.5}$ (d–f) at night during three periods, colored by RH. The red solid line was obtained by a linear fit to the scatters. The time resolution was 1 hour.

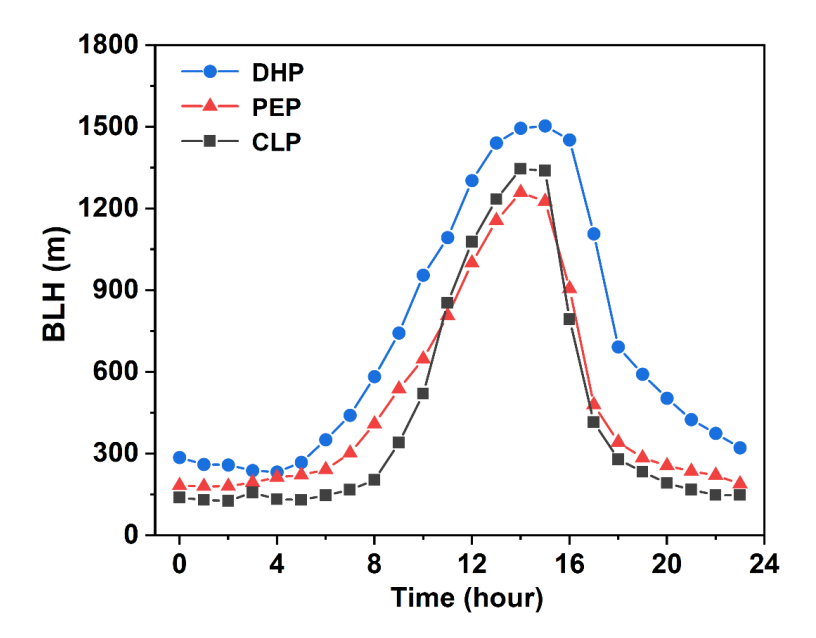


Figure S8 The diurnal variations of the boundary layer height (BLH) during three periods. The blue, red, and black dotted line graphs represent DHP, PEP and CLP, respectively.

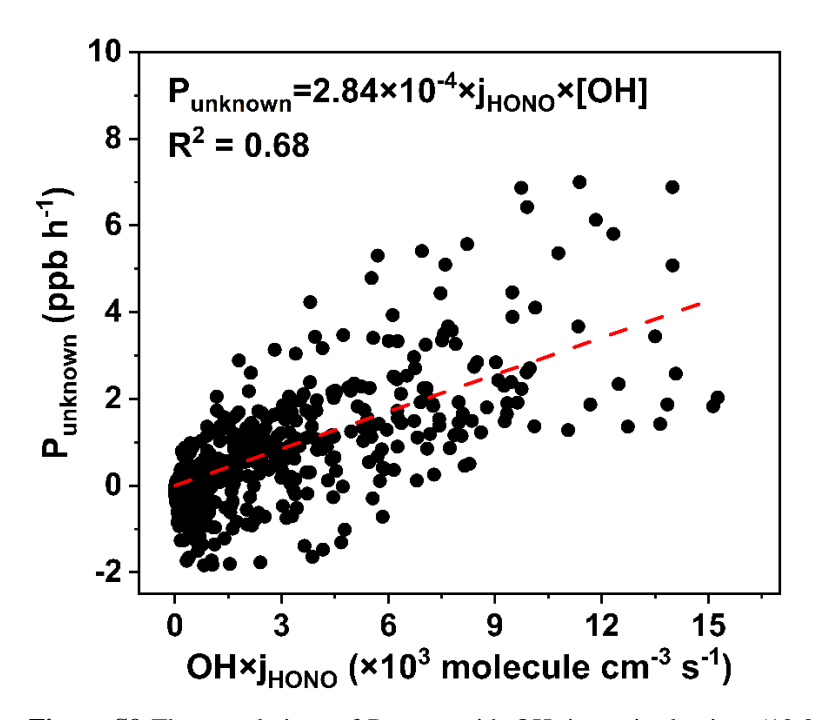


Figure S9 The correlations of $P_{unknown}$ with $OH \times j_{HONO}$ in daytime (10:00–15:00 LT). The red dashed lines were obtained by the linear fits from the scatters data. The data had a temporal resolution of 1 hour.

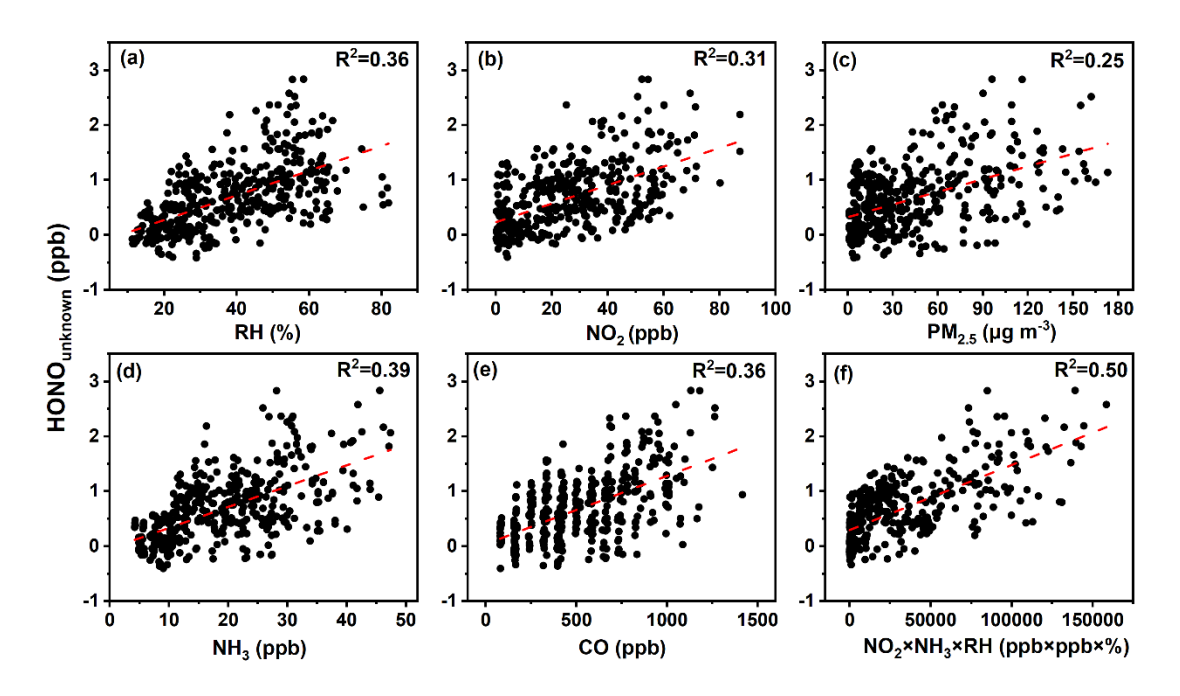


Figure S10 The correlations of $HONO_{unknown}$ with RH, NO_2 , $PM_{2.5}$, NH_3 , CO, and $NO_2 \times NH_3 \times RH$ in nighttime (22:00–03:00 LT). The red dashed lines were obtained by the linear fits from the scatters data. The data had a temporal resolution of 1 hour.

Table S1 Hourly average concentrations of meteorological parameters (Temp, RH, WS, j_{HONO}), chemical species (HONO, O₃, NO, NO₂, NH₃, CO, SO₂, PM_{2.5}) and HONO_{corr}/NO₂ during double-high period, cyclic-haze period and clean period.

Parameters	DHP	PEP	CLP
Temp (°C)	22.87 ± 4.12	13.07 ± 4.28	0.02 ± 4.45
RH (%)	40.71 ± 18.45	39.60 ± 17.23	19.94 ± 6.40
WS (m s ⁻¹)	0.61 ± 0.34	0.48 ± 0.25	0.63 ± 0.31
jноnо (×10 ⁻⁴ s ⁻¹)	3.39 ± 4.60	2.27 ± 3.61	1.81 ± 2.89
$j_{O1D} (\times 10^{-6} \text{ s}^{-1})$	4.02 ± 4.86	2.44 ± 2.60	1.57 ± 1.13
$PM_{2.5} (\mu g \; m^{-3})$	46.03 ± 37.85	46.78 ± 44.05	17.17 ± 15.16
$PM_{10} (\mu g m^{-3})$	91.74 ± 58.87	79.14 ± 60.97	49.59 ± 29.22
NO (ppb)	3.25 ± 7.11	10.91 ± 15.69	7.52 ± 10.91
NO ₂ (ppb)	24.79 ± 23.74	23.67 ± 16.94	9.26 ± 9.23
NH ₃ (ppb)	26.15 ± 9.84	19.83 ± 8.80	8.35 ± 2.61
CO (ppm)	0.54 ± 0.26	0.50 ± 0.30	0.26 ± 0.15
SO ₂ (ppb)	1.07 ± 0.59	0.50 ± 0.30	0.89 ± 0.42
HONO (ppb)	1.71 ± 1.08	1.46 ± 0.90	0.50 ± 0.38
O ₃ (ppb)	39.01 ± 32.30	12.32 ± 13.38	14.87 ± 9.53
HONO _{corr} /NO ₂	0.114 ± 0.106	0.086 ± 0.078	0.085 ± 0.105

Table S2 A total of 21 fresh air masses were identified during the observation period in this study.

Number	Date	Local time	R ² (HONO vs. NOx)	ΔΝΟ/ΔΝΟχ	ΔΗΟΝΟ/ΔΝΟχ
1	2022/10/5	04:00:00-04:10:00	0.87	1.28	0.0174
2	2022/10/11	03:00:00-03:15:00	0.99	0.98	0.0051
3	2022/11/1	23:35:00-23:45:00	0.97	1.19	0.0164
4	2022/11/2	00:45:00-00:55:00	0.85	1.08	0.0143
5	2022/11/2	02:15:00-02:35:00	0.94	1.01	0.0206
6	2022/11/5	00:35:00-01:00:00	0.88	0.98	0.0174
7	2022/11/5	02:35:00-03:00:00	0.88	1.13	0.0126
8	2022/11/7	22:00:00-22:10:00	0.96	1.13	0.0113
9	2022/11/8	01:25:00-01:35:00	0.99	1.01	0.0101
10	2022/11/8	02:10:00-02:25:00	0.82	0.94	0.0131
11	2022/11/8	03:10:00-03:25:00	0.99	1.32	0.0131
12	2022/11/8	22:25:00-22:40:00	0.80	1.08	0.0079
13	2022/11/9	03:10:00-03:20:00	0.86	1.15	0.0197
14	2022/11/10	04:20:00-04:30:00	0.96	1.15	0.0193
15	2022/11/16	19:15:00-19:40:00	0.95	1.05	0.0061
16	2022/11/17	20:00:00-20:15:00	0.89	1.06	0.0167
17	2022/12/6	04:05:00-04:55:00	0.94	0.96	0.0194
18	2022/12/15	01:05:00-01:25:00	0.97	1.00	0.0185
19	2022/12/19	05:20:00-05:30:00	0.80	1.34	0.0210
20	2022/12/19	05:45:00-05:55:00	0.93	1.10	0.0139
21	2022/12/20	04:50:00-05:00:00	0.99	1.03	0.0085

Table S3 Sensitivity study with EF uncertainty for HONO formation processes.

EF	DHP	PEP	CLP
3	-3.2 %	-3.4 %	-2.1%
300	31.5 %	34.1 %	20.5 %

References

Alicke, B.: Impact of nitrous acid photolysis on the total hydroxyl radical budget during the Limitation of Oxidant Production/Pianura Padana Produzione di Ozono study in Milan, J. Geophys. Res. Atmos., 107, https://doi.org/10.1029/2000jd000075, 2002.

Baergen, A. M. and Donaldson, D. J.: Photochemical renoxification of nitric acid on real urban grime, Environ. Sci. Technol., 47, 815-820, https://doi.org/10.1021/es3037862, 2013.

Cai, R., Yang, D., Fu, Y., Wang, X., Li, X., Ma, Y., Hao, J., Zheng, J., and Jiang, J.: Aerosol surface area concentration: a governing factor in new particle formation in Beijing, Atmos. Chem. Phys., 17, 12327-12340, https://doi.org/10.5194/acp-17-12327-2017, 2017.

Colussi, A. J., Enami, S., Yabushita, A., Hoffmann, M. R., Liu, W. G., Mishra, H., and Goddard, W. A., 3rd: Tropospheric aerosol as a reactive intermediate, Faraday Discuss., 165, 407-420, https://doi.org/10.1039/c3fd00040k, 2013.

George, C., Strekowski, R. S., Kleffmann, J., Stemmler, K., and Ammann, M.: Photoenhanced uptake of gaseous NO₂ on solid-organic compounds: a photochemical source of HONO, Faraday Discuss., 130, 195-210, https://doi.org/10.1039/b417888m, 2005.

Ghahremanloo, M., Lops, Y., Choi, Y., and Yeganeh, B.: Deep learning estimation of daily ground-level NO₂ concentrations from remote sensing data, J. Geophys. Res. Atmos.,126, e2021JD034925, https://doi.org/https://doi.org/10.1029/2021JD034925, 2021.

Harrison, R. M., Peak, J. D., and Collins, G. M.: Tropospheric cycle of nitrous acid, J. Geophys. Res. Atmos., 101, 14429-14439, https://doi.org/10.1029/96jd00341, 1996.

He, S., Wang, S., Zhang, S., Zhu, J., Sun, Z., Xue, R., and Zhou, B.: Vertical distributions of atmospheric HONO and the corresponding OH radical production by photolysis at the suburb area of Shanghai, China, Sci. Total Environ., 858, 159703, https://doi.org/10.1016/j.scitotenv.2022.159703, 2023.

Hu, B., Chen, G., Chen, J., Xu, L., Fan, X., Hong, Y., Li, M., Lin, Z., Huang, M., Zhang, F., and Wang, H.: The effect of nitrous acid (HONO) on ozone formation during pollution episodes in southeastern China: Results from model improvement and mechanism insights, Sci. Total Environ., 891, 164477, https://doi.org/https://doi.org/10.1016/j.scitotenv.2023.164477, 2023.

Kebabian, P. L., Wood, E. C., Herndon, S. C., and Freedman, A.: A practical alternative to chemiluminescence-based detection of nitrogen dioxide Cavity attenuated phase shift spectroscopy,

Environ. Sci. Technol., 42, 6040–6045, https://doi.org/10.1021/es703204j, 2008.

Kleffmann, J., Becker, K. H., and Wiesen, P.: Heterogeneous NO₂ conversion processes on acid surfaces: Possible atmospheric implications, Atmos. Environ., 32, 2721-2729, https://doi.org/10.1016/s1352-2310(98)00065-x, 1998.

Kurtenbach, R., Becker, K. H., Gomes, J. A. G., Kleffmann, J., Lorzer, J. C., Spittler, M., Wiesen, P., Ackermann, R., Geyer, A., and Platt, U.: Investigations of emissions and heterogeneous formation of HONO in a road traffic tunnel, Atmos. Environ., 35, 3385-3394, https://doi.org/10.1016/s1352-2310(01)00138-8, 2001.

Lee, J. D., Whalley, L. K., Heard, D. E., Stone, D., Dunmore, R. E., Hamilton, J. F., Young, D. E., Allan, J. D., Laufs, S., and Kleffmann, J.: Detailed budget analysis of HONO in central London reveals a missing daytime source, Atmos. Chem. Phys., 16, 2747-2764, https://doi.org/10.5194/acp-16-2747-2016, 2016.

Li, X., Brauers, T., Häseler, R., Bohn, B., Fuchs, H., Hofzumahaus, A., Holland, F., Lou, S., Lu, K. D., Rohrer, F., Hu, M., Zeng, L. M., Zhang, Y. H., Garland, R. M., Su, H., Nowak, A., Wiedensohler, A., Takegawa, N., Shao, M., and Wahner, A.: Exploring the atmospheric chemistry of nitrous acid (HONO) at a rural site in Southern China, Atmos. Chem. Phys., 12, 1497-1513, https://doi.org/10.5194/acp-12-1497-2012, 2012.

Li, Y., Wang, X., Wu, Z., Li, L., Wang, C., Li, H., Zhang, X., Zhang, Y., Li, J., Gao, R., Xue, L., Mellouki, A., Ren, Y., and Zhang, Q.: Atmospheric nitrous acid (HONO) in an alternate process of haze pollution and ozone pollution in urban Beijing in summertime: Variations, sources and contribution to atmospheric photochemistry, Atmos. Res., 260, https://doi.org/10.1016/j.atmosres.2021.105689, 2021.

Liu, T., Hong, Y., Li, M., Xu, L., Chen, J., Bian, Y., Yang, C., Dan, Y., Zhang, Y., Xue, L., Zhao, M., Huang, Z., and Wang, H.: Atmospheric oxidation capacity and ozone pollution mechanism in a coastal city of southeastern China: analysis of a typical photochemical episode by an observation-based model, Atmos. Chem. Phys., 22, 2173-2190, https://doi.org/10.5194/acp-22-2173-2022, 2022.

Liu, Y., Nie, W., Xu, Z., Wang, T., Wang, R., Li, Y., Wang, L., Chi, X., and Ding, A.: Semi-quantitative understanding of source contribution to nitrous acid (HONO) based on 1 year of continuous observation at the SORPES station in eastern China, Atmos. Chem. Phys., 19, 13289-13308, https://doi.org/10.5194/acp-19-13289-2019, 2019.

Liu, Y. H., Lu, K. D., Ma, Y. F., Yang, X. P., Zhang, W. B., Wu, Y. S., Peng, J. F., Shuai, S. J., Hu, M., and Zhang, Y. H.: Direct emission of nitrous acid (HONO) from gasoline cars in China determined by vehicle chassis dynamometer experiments, Atmos. Environ., 169, 89-96, https://doi.org/10.1016/j.atmosenv.2017.07.019, 2017.

Meng, F. H., Qin, M., Tang, K., Duan, J., Fang, W., Liang, S. X., Ye, K. D., Xie, P. H., Sun, Y. L., Xie, C. H., Ye, C. X., Fu, P. Q., Liu, J. G., and Liu, W. Q.: High-resolution vertical distribution and sources of HONO and NO₂ in the nocturnal boundary layer in urban Beijing, China, Atmos. Chem. Phys., 20, 5071-5092, https://doi.org/10.5194/acp-20-5071-2020, 2020.

Meng, Z. Y., Lin, W. L., Jiang, X. M., Yan, P., Wang, Y., Zhang, Y. M., Jia, X. F., and Yu, X. L.: Characteristics of atmospheric ammonia over Beijing, China, Atmos. Chem. Phys., 11, 6139-6151, https://doi.org/10.5194/acp-11-6139-2011, 2011.

Rappengluck, B., Lubertino, G., Alvarez, S., Golovko, J., Czader, B., and Ackermann, L.: Radical precursors and related species from traffic as observed and modeled at an urban highway junction, J Air Waste Manag Assoc, 63, 1270-1286, https://doi.org/10.1080/10962247.2013.822438, 2013.

Ryan, R. G., Rhodes, S., Tully, M., Wilson, S., Jones, N., Friess, U., and Schofield, R.: Daytime HONO, NO₂ and aerosol distributions from MAX-DOAS observations in Melbourne, Atmos. Chem. Phys., 18, 13969-13985, https://doi.org/10.5194/acp-18-13969-2018, 2018.

Romer, P., Wooldridge, P. J., Crounse, J. D., Kim, M. J., Wennberg, P. O., Dibb, J., Scheuer, E., Blake, D. R., Meinardi, S., Brosius, A. L., Thames, A. B., Miller, D. O., Brune, W. H., Hall, S. R., Ryerson, T. B., and Cohen, R. C. C.: Constraints on aerosol nitrate photolysis as a potential source of HONO and NOx, Environ. Sci. Technol., https://doi.org/10.1021/acs.est.8b03861, 2018.

Su, H., Cheng, Y. F., Cheng, P., Zhang, Y. H., Dong, S., Zeng, L. M., Wang, X., Slanina, J., Shao, M., and Wiedensohler, A.: Observation of nighttime nitrous acid (HONO) formation at a non-urban site during PRIDE-PRD2004 in China, Atmos. Environ., 42, 6219-6232, https://doi.org/10.1016/j.atmosenv.2008.04.006, 2008a.

Su, H., Cheng, Y. F., Cheng, P., Zhang, Y. H., Dong, S. F., Zeng, L. M., Wang, X. S., Slanina, J., Shao, M., and Wiedensohler, A.: Observation of nighttime nitrous acid (HONO) formation at a non-urban site during PRIDE-PRD2004 in China, Atmos. Environ., 42, 6219-6232, https://doi.org/10.1016/j.atmosenv.2008.04.006, 2008b.

Sun, K., Tao, L., Miller, D. J., Pan, D., Golston, L. M., Zondlo, M. A., Griffin, R. J., Wallace, H. W., Leong, Y. J., Yang, M. M., Zhang, Y., Mauzerall, D. L., and Zhu, T.: Vehicle Emissions as an Important Urban Ammonia Source in the United States and China, Environ. Sci. Technol., 51, 2472-2481, https://doi.org/10.1021/acs.est.6b02805, 2017.

Villena, G., Bejan, I., Kurtenbach, R., Wiesen, P., and Kleffmann, J.: Interferences of commercial NO₂ instruments in the urban atmosphere and in a smog chamber, Atmos. Meas. Tech., 5, 149-159, https://doi.org/10.5194/amt-5-149-2012, 2012.

Wang, H., Lyu, X., Guo, H., Wang, Y., Zou, S., Ling, Z., Wang, X., Jiang, F., Zeren, Y., Pan, W., Huang, X., and Shen, J.: Ozone pollution around a coastal region of South China Sea: interaction between marine and continental air, Atmos. Chem. Phys., 18, 4277-4295, https://doi.org/10.5194/acp-18-4277-2018, 2018.

Wang, J., Zhang, X., Guo, J., Wang, Z., and Zhang, M.: Observation of nitrous acid (HONO) in Beijing, China: Seasonal variation, nocturnal formation and daytime budget, Sci. Total Environ., 587-588, 350-359, https://doi.org/10.1016/j.scitotenv.2017.02.159, 2017a.

Wang, T., Xue, L. K., Brimblecombe, P., Lam, Y. F., Li, L., and Zhang, L.: Ozone pollution in China: A review of concentrations, meteorological influences, chemical precursors, and effects, Sci. Total Environ., 575, 1582-1596, https://doi.org/10.1016/j.scitotenv.2016.10.081, 2017b.

Wong, K. W., Oh, H. J., Lefer, B. L., Rappenglueck, B., and Stutz, J.: Vertical profiles of nitrous acid in the nocturnal urban atmosphere of Houston, TX, Atmos. Chem. Phys., 11, 3595-3609, https://doi.org/10.5194/acp-11-3595-2011, 2011.

Wu, D., Zhang, J., Wang, M., An, J., Wang, R., Haider, H., Xu-Ri, Huang, Y., Zhang, Q., Zhou, F., Tian, H., Zhang, X., Deng, L., Pan, Y., Chen, X., Yu, Y., Hu, C., Wang, R., Song, Y., Gao, Z., Wang, Y., Hou, L., and Liu, M.: Global and Regional Patterns of Soil Nitrous Acid Emissions and Their Acceleration of Rural Photochemical Reactions, J. Geophys. Res. Atmos., 127, https://doi.org/10.1029/2021JD036379 10.1029/2021jd036379, 2022.

Xing, C., Liu, C., Hu, Q., Fu, Q., Wang, S., Lin, H., Zhu, Y., Wang, S., Wang, W., Javed, Z., Ji, X., and Liu, J.: Vertical distributions of wintertime atmospheric nitrogenous compounds and the corresponding OH radicals production in Leshan, southwest China, J. Environ. Sci., 105, 44-55, https://doi.org/10.1016/j.jes.2020.11.019, 2021.

Xu, J., Lu, M., Guo, Y., Zhang, L., Chen, Y., Liu, Z., Zhou, M., Lin, W., Pu, W., Ma, Z., Song, Y., Pan, Y., Liu, L., and Ji, D.: Summertime Urban Ammonia Emissions May Be Substantially Underestimated in Beijing, China, Environ. Sci. Technol., 57, 13124-13135, https://doi.org/10.1021/acs.est.3c05266, 2023.

Xu, Q., Wang, S., Jiang, J., Bhattarai, N., Li, X., Chang, X., Qiu, X., Zheng, M., Hua, Y., and Hao, J.: Nitrate dominates the chemical composition of PM_{2.5} during haze event in Beijing, China, Sci. Total Environ., 689, 1293-1303, https://doi.org/https://doi.org/10.1016/j.scitotenv.2019.06.294, 2019.

Xu, Z., Wang, T., Wu, J., Xue, L., Chan, J., Zha, Q., Zhou, S., Louie, P. K. K., and Luk, C. W. Y.: Nitrous acid (HONO) in a polluted subtropical atmosphere: Seasonal variability, direct vehicle emissions and heterogeneous production at ground surface, Atmos. Environ., 106, 100-109, https://doi.org/10.1016/j.atmosenv.2015.01.061, 2015.

Xuan, H., Zhao, Y., Ma, Q., Chen, T., Liu, J., Wang, Y., Liu, C., Wang, Y., Liu, Y., Mu, Y., and He, H.: Formation mechanisms and atmospheric implications of summertime nitrous acid (HONO) during clean, ozone pollution and double high-level PM_{2.5} and O₃ pollution periods in Beijing, Sci. Total Environ., 857, 159538, https://doi.org/10.1016/j.scitotenv.2022.159538, 2023.

Xuan, H., Liu, J., Zhao, Y., Cao, Q., Chen, T., Wang, Y., Liu, Z., Sun, X., Li, H., Zhang, P., Chu, B., Ma, Q., and He, H.: Relative humidity driven nocturnal HONO formation mechanism in autumn haze events of Beijing, npj Clim. Atmos. Sci., 7, https://doi.org/10.1038/s41612-024-00745-8, 2024.

Xue, C., Ye, C., Kleffmann, J., Zhang, W., He, X., Liu, P., Zhang, C., Zhao, X., Liu, C., Ma, Z., Liu, J., Wang, J., Lu, K., Catoire, V., Mellouki, A., and Mu, Y.: Atmospheric measurements at Mt. Tai – Part II: HONO budget and radical ($RO_x + NO_3$) chemistry in the lower boundary layer, Atmos. Chem. Phys., 22, 1035-1057, https://doi.org/10.5194/acp-22-1035-2022, 2022.

Xue, C., Ye, C., Zhang, C., Catoire, V., Liu, P., Gu, R., Zhang, J., Ma, Z., Zhao, X., Zhang, W., Ren, Y., Krysztofiak, G., Tong, S., Xue, L., An, J., Ge, M., Mellouki, A., and Mu, Y.: Evidence for Strong HONO Emission from Fertilized Agricultural Fields and its Remarkable Impact on Regional O₃ Pollution in the Summer North China Plain, ACS Earth Space Chem., https://doi.org/10.1021/acsearthspacechem.0c00314, 2021.

Xue, C., Zhang, C., Ye, C., Liu, P., Catoire, V., Krysztofiak, G., Chen, H., Ren, Y., Zhao, X., Wang, J., Zhang, F., Zhang, C., Zhang, J., An, J., Wang, T., Chen, J., Kleffmann, J., Mellouki, A., and Mu, Y.:

HONO Budget and Its Role in Nitrate Formation in the Rural North China Plain, Environ. Sci. Technol., 54, 11048-11057, https://doi.org/10.1021/acs.est.0c01832, 2020.

Yang, Q., Su, H., Li, X., Cheng, Y. F., Lu, K. D., Cheng, P., Gu, J. W., Guo, S., Hu, M., Zeng, L. M., Zhu, T., and Zhang, Y. H.: Daytime HONO formation in the suburban area of the megacity Beijing, China, Sci. China-Chem., 57, 1032-1042, https://doi.org/10.1007/s11426-013-5044-0, 2014.

Ye, C., Heard, D. E., and Whalley, L. K.: Evaluation of Novel Routes for NOx Formation in Remote Regions, Environ. Sci. Technol., 51, 7442-7449, https://doi.org/10.1021/acs.est.6b06441, 2017.

Ye, C., Zhou, X., Pu, D., Stutz, J., Festa, J., Spolaor, M., Tsai, C., Cantrell, C., Mauldin, R. L., 3rd, Campos, T., Weinheimer, A., Hornbrook, R. S., Apel, E. C., Guenther, A., Kaser, L., Yuan, B., Karl, T., Haggerty, J., Hall, S., Ullmann, K., Smith, J. N., Ortega, J., and Knote, C.: Rapid cycling of reactive nitrogen in the marine boundary layer, Nature, 532, 489-491, https://doi.org/10.1038/nature17195, 2016. Yu, C., Huang, L., Xue, L., Shen, H., Li, Z., Zhao, M., Yang, J., Zhang, Y., Li, H., Mu, J., and Wang, W.: Photoenhanced Heterogeneous Uptake of NO₂ and HONO Formation on Authentic Winter Time Urban Grime, ACS Earth Space Chem., 6, 1960-1968, https://doi.org/10.1021/acsearthspacechem.2c00054, 2022a.

Yu, Y., Cheng, P., Li, H., Yang, W., Han, B., Song, W., Hu, W., Wang, X., Yuan, B., Shao, M., Huang, Z., Li, Z., Zheng, J., Wang, H., and Yu, X.: Budget of nitrous acid (HONO) at an urban site in the fall season of Guangzhou, China, Atmos. Chem. Phys., 22, 8951-8971, https://doi.org/10.5194/acp-22-8951-2022, 2022b.

Yun, H., Wang, Z., Zha, Q. Z., Wang, W. H., Xue, L. K., Zhang, L., Li, Q. Y., Cui, L., Lee, S. C., Poon, S. C. N., and Wang, T.: Nitrous acid in a street canyon environment: Sources and contributions to local oxidation capacity, Atmos. Environ., 167, 223-234, https://doi.org/10.1016/j.atmosenv.2017.08.018, 2017.

Zhang, J., Lian, C., Wang, W., Ge, M., Guo, Y., Ran, H., Zhang, Y., Zheng, F., Fan, X., Yan, C., Daellenbach, K. R., Liu, Y., Kulmala, M., and An, J.: Amplified role of potential HONO sources in O₃ formation in North China Plain during autumn haze aggravating processes, Atmos. Chem. Phys., 22, 3275-3302, https://doi.org/10.5194/acp-22-3275-2022, 2022a.

Zhang, W., Tong, S., Jia, C., Wang, L., Liu, B., Tang, G., Ji, D., Hu, B., Liu, Z., Li, W., Wang, Z., Liu, Y., Wang, Y., and Ge, M.: Different HONO Sources for Three Layers at the Urban Area of Beijing, Environ. Sci. Technol., 54, 12870-12880, https://doi.org/10.1021/acs.est.0c02146, 2020.

Zhang, W., Tong, S., Jia, C., Ge, M., Ji, D., Zhang, C., Liu, P., Zhao, X., Mu, Y., Hu, B., Wang, L., Tang, G., Li, X., Li, W., and Wang, Z.: Effect of Different Combustion Processes on Atmospheric Nitrous Acid Formation Mechanisms: A Winter Comparative Observation in Urban, Suburban and Rural Areas of the North China Plain, Environ. Sci. Technol., 56, 4828-4837, https://doi.org/10.1021/acs.est.1c07784, 2022b.

Zhang, X., Tong, S., Jia, C., Zhang, W., Wang, Z., Tang, G., Hu, B., Liu, Z., Wang, L., Zhao, P., Pan, Y., and Ge, M.: Elucidating HONO formation mechanism and its essential contribution to OH during haze events, npj Clim. Atmos. Sci., 6, https://doi.org/10.1038/s41612-023-00371-w, 2023.

Zhang, X., Tong, S., Jia, C., Zhang, W., Li, J., Wang, W., Sun, Y., Wang, X., Wang, L., Ji, D., Wang, L., Zhao, P., Tang, G., Xin, J., Li, A., and Ge, M.: The Levels and Sources of Nitrous Acid (HONO) in Winter of Beijing and Sanmenxia, J. Geophys. Res. Atmos., 127, https://doi.org/10.1029/2021jd036278, 2022c.

Zhu, Y., Liu, W., Fang, J. Y., Xie, P., Dou, K., Qin, M., and Si, F.: Monitoring and Analysis of Vertical Profile of Atmospheric HONO, NO₂ in Boundary Layer of Beijing, Spectrosc. Spectr. Anal., 31, 1078-1082, https://doi.org/10.3964/j.issn.1000-0593(2011)04-1078-05, 2011.